The Astrophysical Journal, 665:599–607, 2007 August 10

SWIFT OBSERVATIONS OF GRB 070110: AN EXTRAORDINARY X-RAY AFTERGLOW POWERED BY THE CENTRAL ENGINE

E. Troja,[1,2,3] G. Cusumano,[1] P. T. O'Brien,[2] B. Zhang,[4] B. Sbarufatti,[1] V. Mangano,[1] R. Willingale,[2] G. Chincarini,[5,6] J. P. Osborne,[2] F. E. Marshall,[7] D. N. Burrows,[8] S. Campana,[6] N. Gehrels,[7] C. Guidorzi,[5,6] H. A. Krimm,[7,9] V. La Parola,[1] E. W. Liang,[4,10] T. Mineo,[1] A. Moretti,[6] K. L. Page,[2] P. Romano,[5,6] G. Tagliaferri,[6] B. B. Zhang,[4,11] M. J. Page,[12] and P. Schady[12]

Received 2007 February 7; accepted 2007 April 27

ABSTRACT

We present a detailed analysis of *Swift* multiwavelength observations of GRB 070110 and its remarkable afterglow. The early X-ray light curve, interpreted as the tail of the prompt emission, displays a spectral evolution already seen in other gamma-ray bursts. The optical afterglow shows a shallow decay up to ~2 days after the burst, which is not consistent with standard afterglow models. The most intriguing feature is a very steep decay in the X-ray flux at $\sim 2 \times 10^4$ s after the burst, ending an apparent plateau. The abrupt drop of the X-ray light curve rules out an external shock as the origin of the plateau in this burst and implies long-lasting activity of the central engine. The temporal and spectral properties of the plateau phase point toward a continuous central engine emission rather than the episodic emission of X-ray flares. We suggest that the observed X-ray plateau is powered by a spinning-down central engine, possibly a millisecond pulsar, which dissipates energy at an internal radius before depositing energy into the external shock.

Subject headings: gamma rays: bursts — X-rays: individual (GRB 070110)

Online material: color figures

1. INTRODUCTION

The *Swift Gamma-Ray Burst Explorer* (Gehrels et al. 2004) is a multiwavelength observatory specifically designed to study gamma-ray burst (GRB) evolution from their early stages. It is equipped with a wide-field instrument, the Burst Alert Telescope (BAT; Barthelmy et al. 2005a), covering the 15–350 keV energy band, and two narrow-field instruments, the X-Ray Telescope (XRT; Burrows et al. 2005a) and the Ultraviolet/Optical Telescope (UVOT; Roming et al. 2005), covering the 0.2–10 keV band and the 1700–6500 Å wavelength range, respectively.

During the first two years of its mission *Swift* detected ~200 bursts, providing well-sampled X-ray and optical afterglow light curves. Nousek et al. (2006) and Zhang et al. (2006) identified a common pattern in the X-ray light curves, described as consisting of three power-law segments: an early steep decay with a temporal slope $3 \leq \alpha \leq 5$ lasting up to ~300 s, followed by a shallower phase ($0.5 \leq \alpha \leq 1$); the slope of the light curve steepens again ($1.0 \leq \alpha \leq 1.5$) at $\sim 10^3$–10^4 s after the burst onset. X-ray flares, overlaid on the underlying power-law decay, have been detected up to 10^5 s after the BAT trigger (Burrows et al. 2005b; Chincarini et al. 2007).

O'Brien et al. (2006) modeled the observed shape of early X-ray light curves with an exponential decay that relaxes into a power law and, in most cases, presents the shallow phase. They showed that the initial rapid decay is a smooth extension of the prompt emission, probably due to emission from large angles relative to the observer's line of sight (Kumar & Panaitescu 2000). A long-lasting energy injection into the forward shock, due either to a late internal activity or to a radial distribution of Lorentz factors, has been invoked to interpret the shallower stage of the X-ray light curve (Rees & Mészáros 1998; Zhang & Mészáros 2002b; Granot & Kumar 2006). This explanation is consistent with the final smooth steepening into the "standard afterglow" decay (Mészáros & Rees 1997).

The afterglow of GRB 070110 cannot be easily traced back to this well-known scenario. Its early X-ray light curve seems to display a canonical shape, with an initial steep decay and then a very flat plateau phase ($\alpha \sim 0.05$), but $\sim 2 \times 10^4$ s after the trigger the count rate drops abruptly by more than 1 order of magnitude with a slope $\alpha > 7$ (Sbarufatti et al. 2007; Krimm et al. 2007a). The behavior of the optical afterglow seen by the UVOT is very different, showing a shallow smooth decay remaining fairly bright at later times. In the light of the unique properties of its afterglow, the *Swift* team identified GRB 070110 as a "burst of interest" encouraging a follow-up campaign (Krimm et al. 2007b).

The optical afterglow of GRB 070110 (Krimm et al. 2007a) was also detected by the ESO VLT equipped with the FORS2 instrument. A redshift of $z = 2.352 \pm 0.001$ has been inferred on the basis of several absorption features in the spectra (Jaunsen et al. 2007). Further VLT observations, performed ~10.7 days

[1] INAF-Istituto di Astrofisica Spaziale e Fisica Cosmica, Sezione di Palermo, via Ugo la Malfa 153, 90146 Palermo, Italy.
[2] Department of Physics and Astronomy, University of Leicester, Leicester LE1 7RH, UK.
[3] Dipartimento di Scienze Fisiche ed Astronomiche, Sezione di Astronomia, Università di Palermo, Piazza del Parlamento 1, 90134 Palermo, Italy.
[4] Department of Physics and Astronomy, University of Nevada, Las Vegas, NV 89154.
[5] Università degli studi di Milano-Bicocca, Dipartimento di Fisica, piazza delle Scienze 3, I-20126 Milan, Italy.
[6] INAF-Osservatorio Astronomico di Brera, via Emilio Bianchi 46, I-23807 Merate (LC), Italy.
[7] NASA Goddard Space Flight Center, Greenbelt, MD 20771.
[8] Department of Astronomy and Astrophysics, 525 Davey Laboratory, Pennsylvania State University, University Park, PA 16802.
[9] Universities Space Research Association, 10211 Wincopin Circle, Suite 500, Columbia, MD 20144.
[10] Department of Physics, Guangxi University, Nanning 530004, China.
[11] National Astronomical Observatories/Yunnan Observatory, Chinese Academy of Sciences, Kunming 650011, China.
[12] Mullard Space Science Laboratory, University College London, Holmbury St. Mary, Dorking, Surrey RH5 6NT, UK.

after the burst, detected a fainter than predicted afterglow, suggesting the presence of an optical break (Malesani et al. 2007a).

In this paper we report on the gamma-ray, X-ray, and optical observations performed by *Swift*. The paper is organized as follows: in § 2 we present a multiwavelength timing and spectral analysis of both the prompt and the afterglow emission; in § 3 we discuss our results. Finally, in § 4 we summarize our findings and conclusions.

Throughout the paper, times are given relative to the BAT trigger time T_0, $t = T - T_0$, and the convention $F_{\nu,t} \propto \nu^{-\beta} t^{-\alpha}$ has been followed, where the energy index β is related to the photon index $\Gamma = \beta + 1$. We have adopted a standard cosmology model with Hubble constant $H_0 = 70$ km s^{-1} Mpc^{-1} and cosmological constants $\Omega_\Lambda = 0.73$, $\Omega_M = 0.27$ (Spergel et al. 2007). The phenomenology of the burst is presented in the observer time frame, unless otherwise stated. All the quoted errors are given at 90% confidence level for one interesting parameter ($\Delta\chi^2 = 2.706$; Lampton et al. 1976).

2. DATA ANALYSIS

2.1. *Observations*

GRB 070110 triggered the *Swift* BAT at 07:22:41 UT on 2007 January 10. The *Swift* narrow-field instruments, XRT and UVOT, began observing 93 and 85 s after the trigger, respectively. An accurate afterglow position was rapidly determined by the UVOT at R.A. = $00^{\rm h}03^{\rm m}39.20^{\rm s}$, decl. = $-52^\circ 26.3''$ (J2000.0; Krimm et al. 2007a), with an uncertainty of $1''$.

XRT observations began with an initial 2.5 s image mode frame and then, as the source was bright ($\sim$40 counts s^{-1}), data were collected in Window Timing (WT) mode. The XRT automatically switched to Photon Counting (PC) mode when the source decreased to $\sim$2 counts s^{-1}. Follow-up observations lasted 26 days for a total net exposure of 165 s in WT mode and 330 ks in PC mode.

The UVOT took a short exposure with the *V* filter while the spacecraft was settling at the end of the initial slew. This exposure was followed by a "finding chart" exposure with the White filter lasting 100 s and then an exposure with the *V* filter lasting 400 s. UVOT then began its usual procedure of cycling through its three visible filters (*V*, *B*, and *U*) and three UV filters (UVW1, UVM2, and UVW2). The optical afterglow was detected in the White, *U*, *B*, and *V* filters, but not in the UV filters. The lack of detection of the afterglow in the UV filters is consistent with the measured redshift. A total of 219 UVOT exposures were taken in the first 6.7 days, after which the afterglow fell below the detection thresholds.

2.2. *Gamma-Ray Data*

We analyzed BAT event data using the standard BAT analysis software included in the NASA's HEASARC software (HEASOFT, ver. 6.1.2). Figure 1 presents the BAT mask-weighted light curve in the 15–150 keV energy band. It shows a first main peak at $t \sim 0$ s and then a decay on which several peaks are superposed; emission is visible until $t \sim 100$ s. We estimated the burst duration, defined as the interval containing 90% of the total observed fluence, to be $T_{90}(15\text{–}150\ \text{keV}) = 89 \pm 7$ s.

Spectra were created using the task `batbinevt`, updating relevant keywords with `batupdatephakw`. The corresponding response matrices were generated by the task `batdrmgen`. Systematic errors were properly added to the spectra. Since the spacecraft slew started $\sim$40 s after the trigger, we created two different spectra (before and during the slew) with the appropriate response matrices and performed a joint fit.

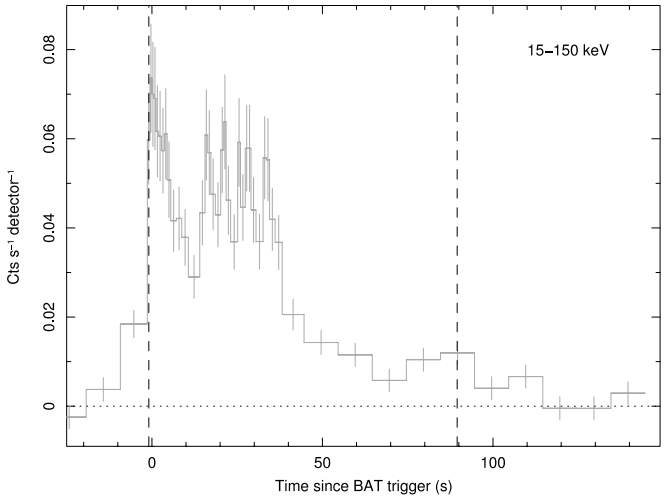

FIG. 1.—BAT mask-weighted light curve (15–150 keV) of GRB 070110. Dashed vertical lines mark the T_{90} duration. [*See the electronic edition of the Journal for a color version of this figure.*]

The time-averaged T_{90} spectrum (from -0.4 to 89 s) can be fitted with a simple power law of photon index 1.57 ± 0.12. A cutoff power law or a Band model (Band et al. 1993) does not provide a better description and cannot constrain the peak energy value. In the hardness ratio light curves, comparing different BAT energy bands, no sign of a significant spectral evolution is present throughout the prompt emission.

The fluence over the 15–150 keV band is $1.8^{+0.2}_{-0.3} \times 10^{-6}$ erg cm^{-2}, from which we derive an observed isotropic energy of 2.3×10^{52} erg. This value can be considered as a lower limit to the isotropic energy, $E_{\gamma,\rm iso}$, which is defined over a larger energy band (1 keV–10 MeV in the source rest frame). Extrapolating our best-fit model over the entire 1 keV–10 MeV (source rest frame), we estimate an upper limit of $E_{\gamma,\rm iso} \leq 1.3 \times 10^{53}$ erg. This value is derived under the extreme assumption that the best description of the spectrum is a Band law (Band et al. 1993) with a peak energy $E_p > 10$ MeV in the source rest frame.

2.3. *X-Ray Data*

XRT data were processed using the XRTDAS software package (ver. 2.0.1) distributed within HEASOFT. We used the latest release of the XRT Calibration Database (CALDB 2.6) and applied standard screening criteria to obtain the final cleaned event list. We selected only events with grades 0–12 for PC mode data and 0–2 for WT mode data. Such a selection provides the best combination of spectral resolution and detection efficiency. Our analysis has been performed over the 0.3–10 keV energy band.

2.3.1. *Temporal Analysis*

We extracted WT data in a rectangular region, 40 pixels $\times$ 20 pixels wide, centered on the source position. The background contribution was estimated from a region, with the same shape and size, sufficiently offset (>2′) from the source position to avoid contamination from the PSF wings and free from contamination by other sources.

The first 300 s of PC observations were affected by pileup. To account for this, we chose an annular extraction region centered on the source, having an inner radius of 4 pixels and an outer radius of 30 pixels. From the second orbit on ($t \geq 3 \times 10^4$ s), when pileup is no longer present, the source count rate was estimated in a circular region with a 30 pixel radius. The count rate evolution in the later observations ($t > 3 \times 10^5$ s) was obtained using

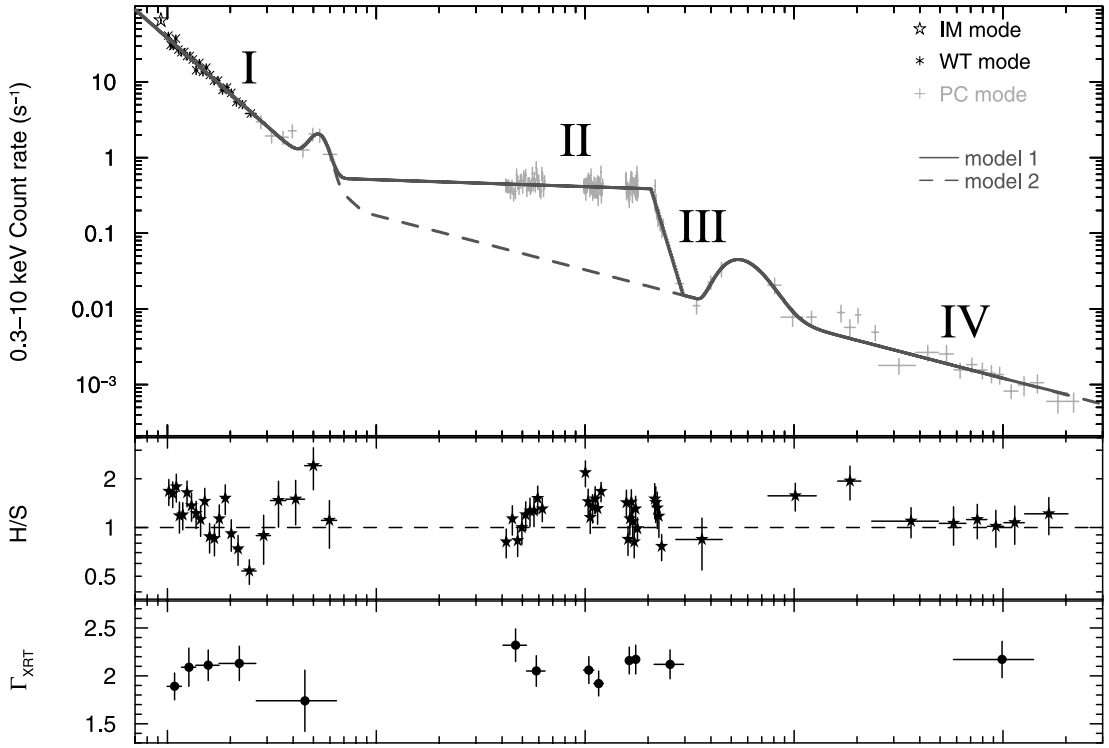

FIG. 2.—*Top*: XRT light curve of GRB 070110 in the 0.3–10 keV band. The two models described in the text are shown: power-law segments with three temporal breaks (*solid line*) and a simple broken power law (*dashed line*). The bump at $t \sim 530$ s is modeled with a Gaussian function, the late one at $t \sim 5 \times 10^4$ s with a FRED profile. The four phases of the X-ray light curve are marked: (I) an early decay, (II) an apparent plateau followed by (III) a rapid drop, and (IV) a final shallow decay. *Middle*: Hardness ratio (H/S) light curve. It compares source counts in the hard band (H; 1–10 keV) and in the soft band (S; 0.3–1 keV). *Bottom*: Photon index $\Gamma_{\rm XRT}$ temporal variations. These values were derived fitting the X-ray spectra with an absorbed power-law model. [*See the electronic edition of the Journal for a color version of this figure.*]

the task `sosta` of the XIMAGE package, using an extraction region that optimizes the signal-to-noise ratio of the detection.

All the light curves presented here are background subtracted and corrected for point-spread function (PSF) losses, vignetting effects, and exposure variations. The 0.3–10 keV light curve is shown in Figure 2 (*top*). WT and PC data were binned to achieve minimum signal-to-noise ratios of 8 and 5, respectively. Late points ($t \geq 10^5$ s) are 3 σ detections. We also included the detection taken in Image Mode, converting digital number (DN) units into count rate (Hill et al. 2006; Mangano et al. 2007b).

The light curve has been modeled with power-law segments of different slopes, whose best-fit parameters are reported in the second column of Table 1. The best-fit model is shown by the solid line in the top panel of Figure 2. We also performed a fit of the light curve with a simple broken power law, excluding from the analysis the plateau and the following steep drop. The model is shown by the dashed line in Figure 2, with best-fit parameters reported in Table 1 (third column).

TABLE 1
RESULTS FROM X-RAY LIGHT CURVE FITS

Parameters	Model 1, Multiple Broken PL	Model 2, Simple Broken PL
α_1	$2.44^{+0.13}_{-0.12}$	$2.45^{+0.13}_{-0.12}$
$t_{\rm break,1}$ (s)	570 ± 50	730^{+270}_{-230}
α_2	$0.09^{+0.07}_{-0.06}$	0.72 ± 0.06
$t_{\rm break,2}$ (ks)	$20.57^{+0.26}_{-0.11}$	...
α_3	$9.0^{+2.8}_{-1.0}$	...
$t_{\rm break,3}$ (ks)	29 ± 2	...
α_4	$0.71^{+0.08}_{-0.09}$	...

NOTE.—Two different models have been considered and they are discussed in the text.

In both models we used a Gaussian function, centered at $t \sim 530$ s and $\sigma \sim 50$ s wide, to model the small bump at the end of the early decay. The fast rise, after the abrupt drop at $\sim 2 \times 10^4$ s, and the following decay are well described by a fast-rise-exponential-decay (FRED) profile, peaking at $t \sim 55$ ks.

The hardness ratio light curve is reported in the middle panel of Figure 2. It is defined as the ratio between the source counts in the hard band (H; 1–10 keV) and the source counts in the soft band (S; 0.3–1 keV). An initial hard-to-soft evolution is present followed by a hardening of the spectrum, which corresponds to the small bump in the X-ray light curve at ~530 s. The hardness ratio shows an increasing trend at the beginning of the observed plateau and spectral variations throughout it. The very steep drop displays a hard-to-soft evolution. Later points ($t \gtrsim 10^5$ s) have a harder spectrum, maybe due to a late flaring activity, as the fluctuations in the light curve suggest. At times later than 2×10^5 s the afterglow evolution does not show any further spectral variation.

2.3.2. *Spectral Analysis*

In order to quantify the spectral variations seen in the hardness ratio light curve, we performed a time-resolved spectral analysis. Source and background spectra were extracted from the same regions used to create light curves (§ 2.3.1). The relevant ancillary response files were generated using the task `xrtmkarf`. Time intervals were selected according to light curve phases and to have at least 400 net counts each. Only the first PC orbit spectrum (from 266 to 644 s) has a lower statistical quality (~200 source counts), due to the presence of pileup. Spectral channels were grouped so as to have at least 20 counts each. The χ^2 statistic was applied.

TABLE 2
Results from X-Ray Spectral Fits

X-Ray Phase	Instrument Mode	Start (s)	Stop (s)	Γ_X	χ^2/dof
Early decay	WT	99.7	117	1.84 ± 0.11	14/21
	WT	117	137	1.92 ± 0.14	23/17
	WT	137	177	2.16 ± 0.14	21/18
	WT	177	265	2.21 ± 0.14	6/14
	PC	266	644	1.7 ± 0.3	7/6
Plateau	PC	4043	5237	2.32 ± 0.17	12/15
	PC	5237	6426	2.05 ± 0.16	21/17
	PC	9825	10997	2.06 ± 0.14	23/16
	PC	10997	12210	1.92 ± 0.13	13/16
	PC	15607	16896	2.16 ± 0.14	28/19
	PC	16896	17993	2.17 ± 0.14	20/17
Drop	PC	21394	29559	2.12 ± 0.15	14/15
Shallow decay[a]	PC	5.8×10^5	1.4×10^6	2.17 ± 0.20	...

Notes.—Spectra were modeled with an absorbed power law. Galactic and intrinsic absorption were kept fixed at values of 1.86×10^{20} and 2.6×10^{21} cm^{-2}, respectively.
[a] The Cash statistic was applied.

All the X-ray spectra can be modeled with an absorbed power law. The Galactic absorption component was kept fixed at a value of 1.86×10^{20} cm^{-2} (Dickey & Lockman 1990); an additional redshifted absorption component, modeling the host intrinsic absorption, was also included. In order to estimate the host absorption we extracted a WT (from 100 to 265 s) and a PC spectrum (from 4 to 30 ks). Since at low energies ($\sim$0.5 keV) XRT spectra may be affected by calibration uncertainties,[13] we performed our analysis excluding energy channels in the range 0.45–0.55 keV. From the joint spectral fit we obtained an intrinsic absorption of $N_H^{host} = (2.6 \pm 1.1) \times 10^{21}$ cm^{-2}. This value was derived assuming a host galaxy with solar metallicity.

We then performed time-resolved spectral fits keeping the absorption fixed as above and leaving only the photon index Γ_X and the normalization as free parameters. We also tested whether the initial softening of the spectrum could be due to a decreasing intrinsic absorption, as previously witnessed in other GRBs (Cusumano et al. 2007; Campana et al. 2006), but the low number of counts did not allow us to constrain the N_H^{host} behavior.

In order to estimate the spectral index during the final shallow decay, we extracted a spectrum in the time interval from 5.8×10^5 to 1.4×10^6 s, using a circular region of 5 pixels radius centered on the source position. Because of the low number of counts ($\sim$120) and the negligible background contamination, the Cash statistic was applied (Cash 1979). We obtained $\Gamma_X = 2.17 \pm 0.20$.

The selected time intervals and results from the spectral fit are listed in Table 2. The photon index variations with time are reported in the bottom panel of Figure 2.

2.4. *Ultraviolet/Optical Data*

Independent measurements of the position of the afterglow were made after summing the images taken during the first day after the trigger for the White, *V*, *B*, and *U* filters. The mean position is R.A. = $00^h03^m39.23^s$, decl. = $-52^\circ58'26.9''$ with an estimated 1 σ uncertainty of $0.25''$ in each direction, based on the rms deviation of the four measurements. This position is consistent with the ground-based position given in Malesani et al. (2007b).

We performed photometry using a circular aperture of radius $2.5''$ centered on the position of the optical afterglow. This choice allows us to minimize the background contribution. Aperture corrections were computed using stars in the images to convert the $2.5''$ photometry to a $6''$ aperture for the *V*, *B*, and *U* filters, and a $12''$ aperture for the White filter. Adjacent exposures with $\Delta T/T < 0.1$ were co-added to improve the signal-to-noise ratio.

The instrumental magnitudes were transformed to Vega magnitudes using the standard photometric zero points in the *Swift* UVOT calibration database.[14] Table 3 contains the results of the UVOT photometry. The reported errors and upper limits (ULs) are at 1 and 3 σ confidence level, respectively.

[13] See http://heasarc.gsfc.nasa.gov/docs/swift/analysis.

[14] See http://heasarc.gsfc.nasa.gov/docs/heasarc/caldb/swift/docs/uvot/index.html.

TABLE 3
Swift UVOT Photometry of GRB 070110 Afterglow

Start (s)	Δt (s)	Magnitude[a]	Error[b]	Filter
103	100	19.90	0.31	White
4249	200	19.18	0.26	White
5681	200	19.69	0.18	White
85	9	17.35	UL	*V*
208	400	20.28	0.45	*V*
4658	200	18.94	0.33	*V*
6091	200	18.83	UL	*V*
22298	18665	20.38	0.27	*V*
161578	47181	21.52	0.32	*V*
4044	1632	20.33	0.30	*B*
11644	598	20.59	0.21	*B*
28983	603	21.32	0.36	*B*
114817	12775	22.08	0.32	*B*
662	15	19.23	0.51	*U*
5272	200	19.63	0.22	*U*
10733	906	19.84	0.14	*U*
17423	602	20.22	0.23	*U*
28072	906	20.42	0.22	*U*
34762	603	20.84	0.31	*U*
235449	135190	22.58	UL[c]	*U*
495668	81911	22.07	UL	*U*

[a] Values are not corrected for extinction.
[b] Errors at the 68% confidence level or 3 σ upper limits (ULs) are given.
[c] Our reanalysis using the refined optical position gives a 3 σ UL instead of the detection quoted in Krimm et al. (2007a).

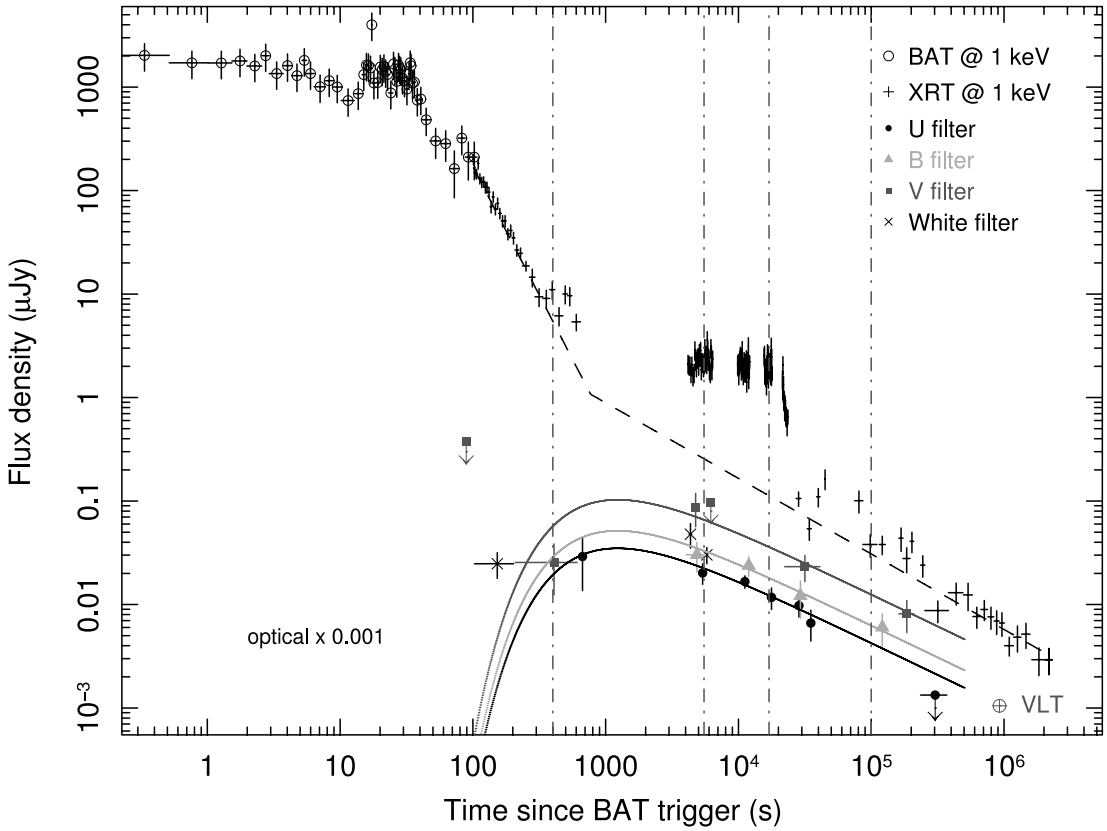

FIG. 3.—Combined BAT, XRT, and UVOT light curves. BAT and XRT count rates were converted into monochromatic fluxes using the results from the spectral analysis. UVOT magnitudes were corrected for the Galactic extinction and converted into flux densities at the central wavelength of each filter. In the plot UVOT flux values have been scaled by a factor 10^{-3}. The optical best-fit models, discussed in the text, are shown by solid lines. The dashed line shows the broken power-law model (model 2). The vertical dash-dotted lines mark the times at which SEDs were computed. [*See the electronic edition of the Journal for a color version of this figure.*]

The Galactic reddening in the burst direction is $E(B-V) = 0.014$ (Schlegel et al. 1998). Using the value from the extinction curve in Pei (1992) for the Milky Way at the central wavelength of each filter, we estimated the extinction for the UVOT filters to be $A_V = 0.04$ mag, $A_B = 0.06$ mag, and $A_U = 0.07$ mag.

Figure 3 presents the multiwavelength light curve of GRB 070110, including gamma-ray, X-ray, and optical data. Both BAT and XRT light curves were converted into flux units using the best-fit spectral models. The *V*, *B*, and *U* magnitudes were corrected for Galactic extinction along the line of sight and then converted to monochromatic fluxes at the central wavelength of each filter. Since the afterglow is not detected blueward of the *U* filter, we took 4450 Å as the effective midwavelength of the White filter. The conversion factor from count rate to monochromatic flux density depends on the afterglow spectral shape and the White filter effective area curve, and it was found to be 0.026 mJy s count^{-1}.

With the exception of the first detection in the *U*, *V*, and White filters, the UVOT light curves show a decaying behavior that can be well described by a simple power law. An independent fit of the three light curves gives the following temporal slopes: $\alpha_V = 0.65 \pm 0.14$, $\alpha_B = 0.53 \pm 0.13$, and $\alpha_U = 0.54 \pm 0.15$. We note that the UVOT late slopes are consistent, within the errors, with the late-time X-ray slope in Table 1. If the late VLT detection in the *V* band reported in Malesani et al. (2007a) is also included in the fit, the slope α_V steepens to 0.88 ± 0.09. Alternatively, we attempted a fit with a broken power law, which gives an initial decay of 0.62 ± 0.16, steepening at $\sim$150 ks to 1.3 ± 0.2. Both models provide a good description of the light curve in the *V* band.

A joint fit of the three UVOT light curves (*U*, *B*, and *V*) has been performed using the functional form of Willingale et al. (2007). We allowed the normalizations to vary independently, tying other parameters. Upper limits and the VLT detection were not considered in the fit. We found that our light curves follow a power-law decay with a common slope of 0.63 ± 0.13.

The best-fit models of the three UVOT light curves (*U*, *B*, and *V*) with the Willingale et al. (2007) function are shown by solid lines in Figure 3. The fast rise of the optical emission is poorly sampled, and we note that the first detection in the White filter suggests a more gentle onset of the afterglow emission. For comparison we report the broken-power-law model (model 2), described in § 2.3.1 (Fig. 3, *dashed line*).

2.5. *Optical/X-Ray Spectral Energy Distributions*

We calculated the spectral energy distribution (SED) at four representative times: $t = 400$ s during the initial decay, $t = 5.5$ and 17 ks at the beginning and end of the plateau phase, and $t = 100$ ks during the shallower decay. The four times are marked by vertical lines in Figure 3.

Figure 4 shows the four SEDs derived from the optical and X-ray light curves. Flux values in the UVOT filters at the selected times are corrected for Galactic extinction (*open symbols*) and were derived from the best-fit models shown in Figure 3. At a redshift of $z = 2.352$ the Lyα forest is present throughout the *U* filter. Therefore, in constructing the SEDs we have corrected the *U*-band count rate for the expected intergalactic Lyα transmission of 86% over the *U* passband (Madau 1995).

X-ray data were converted into flux units for each time selecting the appropriate photon index value from Table 2. X-ray fluxes and their error regions are shown by the black cones. The contribution of the host galaxy to extinction have been estimated as the

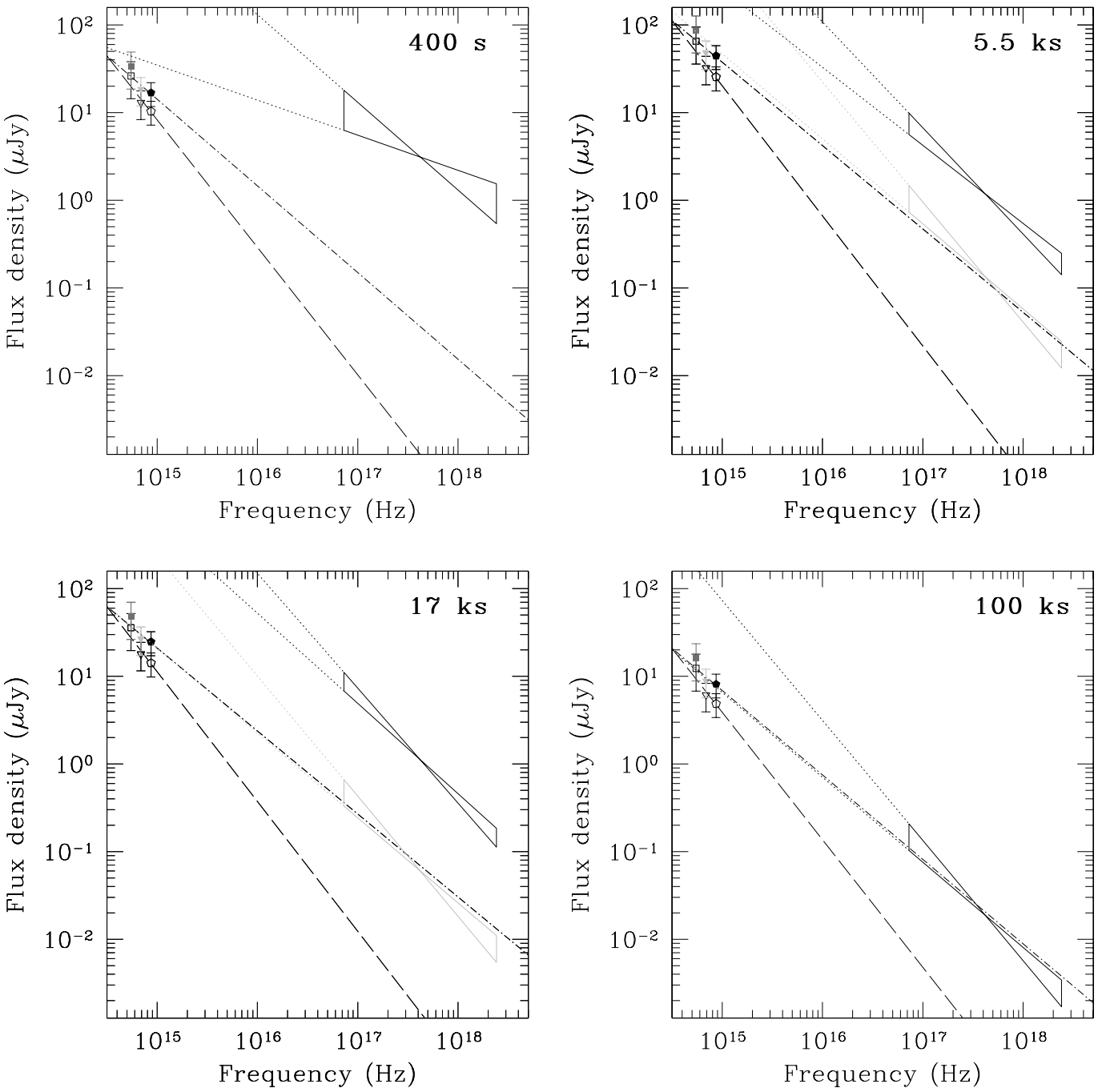

FIG. 4.—Optical, ultraviolet, and X-ray SEDs at 400 s, 5.5 ks, 17 ks, and 100 ks. UVOT points have been corrected for the Galactic extinction $A_V = 0.04$ mag (*open symbols*) and for the host extinction $A_V = 0.08$ mag (*filled symbols*) along the line of sight. The dashed line is the best fit of the optical data corrected only for Galactic extinction. The dot-dashed line is the best fit of the optical data corrected for both the Galactic and the host intrinsic extinctions. The solid black lines define the cone corresponding to the 90% uncertainty on the spectral slope in the X-ray band. This cone is extrapolated to the optical band through the dotted lines. The X-ray fluxes, extrapolated at $t = 5.5$ and 17 ks according to our model 2, and the corresponding error cones are also shown (*gray solid lines*). [*See the electronic edition of the Journal for a color version of this figure.*]

additional extinction required to have optical and X-ray data lying on the same power law at $t = 100$ ks. Accounting for a host extinction of $A_V = 0.08$ mag with the extinction curve for the Small Magellanic Cloud (SMC; Pei 1992) provides a better match between optical and X-ray data. The entire data set at the later times seems consistent with a common physical origin. UVOT fluxes corrected for both the Galactic and the intrinsic extinctions are shown by filled symbols. The best-fit power law of the optical SED is shown by the dot-dashed line.

At early times ($t = 400$ s) the optical data are not consistent with the extrapolation of the X-ray spectrum to low energies. At 5.5 and 17 ks, during the apparent plateau, the optical and X-ray spectral distributions are also completely inconsistent with one another, implying different origins for the optical and X-ray photons.

In § 2.3.1 we have shown that the X-ray light curve, excluding the plateau, can be fitted with a simple two-component broken power law plus flares. Since the slope of this power law is

marginally consistent with that observed in the optical bands, it follows that the SED consistency observed at late times also applies to this component. This is illustrated in Figure 4 (*top right and bottom left*), where we have extrapolated the late-time SED to 5.5 and 17 ks, using light curve model 2 (Table 1, third column) to evaluate the X-ray count rates. These values were derived using the photon index value at late times ($t > 580$ ks). The extrapolated values and their error regions are shown by the gray cones.

If we assume for the host galaxy of GRB 070110 the same gas-to-dust ratio measured in the SMC, $N_{\rm H}/A_V = 1.6 \times 10^{22}$ cm^{-2} mag^{-1} (Weingartner & Draine 2000), an intrinsic hydrogen column density of 1.3×10^{21} cm^{-2} is inferred from the estimated rest-frame visual extinction $A_V = 0.08$ mag.

The intrinsic absorption derived from fitting the X-ray spectra is instead $(1.6 \pm 0.7) \times 10^{22}$ cm^{-2} for an SMC-like absorber, higher than the one expected from the gas-to-dust relationship. We derived the latter absorption value modeling the intrinsic X-ray absorption spectral component with the model `tbvarabs` in XSPEC (Arnaud 1996), keeping the absorber abundances fixed to SMC values ($\sim Z_{\odot}/8$).

The high X-ray absorption column and low optical extinction measured for GRB 070110 require a higher than expected gas-to-dust ratio, and are indicative of an interstellar medium significantly different from the one observed in the local universe. Such difference could be ascribed to the action of the GRB radiation on its immediate environment (Waxman & Draine 2000; Perna et al. 2003) or, alternatively, to an intrinsically higher gas-to-dust ratio in GRB birth sites (Watson et al. 2006). Discrepancies between optical and X-ray extinctions in GRB environments were first found by Galama & Wijers (2001) and then confirmed by subsequent studies on large GRB samples (e.g., Kann et al. 2006; Starling et al. 2007; Tagliaferri et al. 2007).

3. DISCUSSION

3.1. *The Early X-Ray Tail*

As shown in Figure 2 (*top*), the X-ray light curve is composed of four distinct components. It starts with (I) an early steep-decay component with $\alpha = 2.44 \pm 0.13$ following the prompt gamma rays. The early decay is followed by (II) a plateau with an essentially constant flux that extends up to $t \sim 20$ ks. Luminosity fluctuations are seen throughout the plateau phase. Following the plateau is (III) a remarkable steep drop with a temporal index of $\sim$9.0. After this steep fall the afterglow light curve rises again, showing a late flare, then enters (IV) a more normal decay segment with $\alpha \sim 0.7$.

The hardness ratio light curve (Fig. 2, *middle*) shows an initial hard-to-soft spectral evolution during the early decay. Our spectral analysis confirms a softening of the spectral index $\beta_{\rm X}$ from a value of 0.8 to 1.2. The early X-ray decay has been generally interpreted as the prompt emission tail, due to the delay of propagation of photons from high latitudes with respect to the line of sight (Tagliaferri et al. 2005; Nousek et al. 2006; O'Brien et al. 2006; Zhang et al. 2006).

The curvature effect alone, which suggests $\alpha = 2 + \beta$ (Kumar & Panaitescu 2000), cannot explain both the spectral evolution feature and the shallower than expected temporal slope. Such behavior has been seen in other GRBs detected by *Swift*, and as reported by Zhang et al. (2007), spectral evolution seems a common feature in early, bright GRB tails (e.g., GRB 060614; Mangano et al. 2007a). Phenomenological models involving an underlying central engine afterglow with a steep spectral index or an internal shock afterglow with a cooling frequency passing through the XRT window may be candidates for interpreting these spectral evolutions (Zhang et al. 2007).

3.2. *The Plateau Phase*

The observed plateau is a feature of great interest. This component displays an apparently constant intensity extending up to $t \sim 20$ ks, followed by an abrupt drop with a very steep decay index. Compared with the canonical XRT light curve GRBs observed by *Swift* (Nousek et al. 2006; O'Brien et al. 2006; Zhang et al. 2006; Willingale et al. 2007), such a steep decay following a plateau is unique.

In most other *Swift* GRBs, the plateau is followed by a "normal" decay that could be generally interpreted as the standard external forward shock afterglow. The plateau in those cases is therefore consistent with a refreshed shock (Rees & Mészáros 1998; Zhang et al. 2006; Nousek et al. 2006) as the total energy in the blast wave is replenished with time.

The abrupt steep decay in GRB 070110, on the other hand, is inconsistent with an external shock origin of the plateau. This is because, within the external-shock model, it is impossible to produce a decay slope as steep that observed. The steepest possible decay from an external shock occurs after a jet break. The post-jet-break decay slope can be as steep as $\alpha \sim p$, where p is the electron spectral index (Rhoads 1999; Sari et al. 1999), and afterglow modeling suggests that p is typically between 1.5 and 3.

A steep decay may be expected when the blast wave leaves a density clump and falls into a very tenuous medium. In such a case, the curvature effect (Kumar & Panaitescu 2000) defines the decay slope. However, detailed numerical calculations suggest that the zero-time point of the external-shock scenarios cannot substantially be shifted from the GRB trigger time (Zhang et al. 2006; Lazzati & Begelman 2006; Kobayashi & Zhang 2007). As a result, the expected steep decay index within this scenario is $\alpha \sim 2 + \beta \sim 3$, far shallower than the observed value.

By assuming that the steep decay following the plateau is due to the curvature effect, we performed the same test as Liang et al. (2006), who tested the internal origin of X-ray flares. We found that to satisfy the $\alpha = 2 + \beta$ condition the zero time t_0 needs to lie in the range 16–18 ks after the trigger, slightly before the beginning of the abrupt drop. The very steep decay component therefore strongly suggests that the plateau is of *internal* origin, since t_0 is allowed to shift to much later epochs within the internal scenarios (Zhang et al. 2006; Liang et al. 2006).

Several other GRBs have previously shown similar, but not exactly the same, behavior. The afterglow of GRB 051117A (Goad et al. 2007) shows a sharp drop of the X-ray flux at $\sim 10^4$ s, followed by a shallower decay ($\alpha \sim 0.7$). However, in this case the early X-ray light curve seems dominated by flaring activity and it does not show any evident plateau. Figure 5 compares the rest-frame light curves of both GRB 050904 and GRB 070110. GRB 050904 (Cusumano et al. 2006, 2007) shows a remarkably similar behavior to GRB 070110, with a rapid decay following the multiple episodic X-ray flares. However, GRB 070110 displays a much smoother emission episode before the rapid decay. While the steep decay following the flares in GRB 050904 is expected, the drop-off after the plateau in GRB 070110 is not.

On the basis of *Swift* data, collected in portions lasting less than an hour, we cannot definitely rule out that the observed plateau is due to the same mechanism producing erratic X-ray flares in other GRBs, such as GRB 050904. The hardness ratio (Fig. 2, *middle*) appears to rise slowly at the start of the plateau ($\sim$4 ks), and a decreasing trend is visible during the sharp decay ($\sim$20 ks). Such behavior is similar to the one seen in the hardness ratio light curves

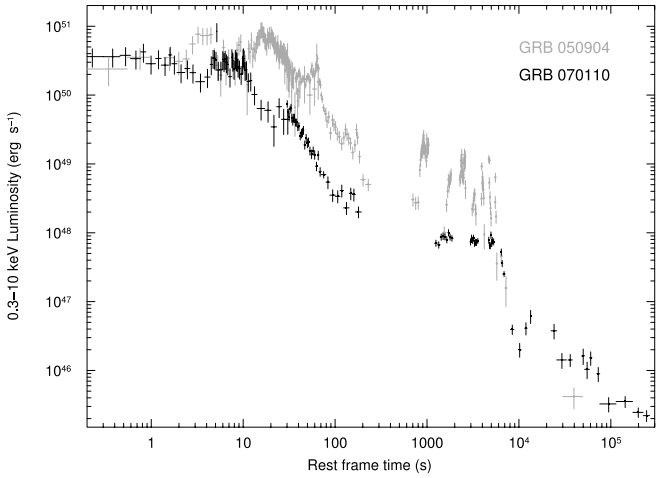

FIG. 5.—Combined BAT and XRT light curves of GRB 050904 ($z = 6.29$) and GRB 070110 ($z = 2.35$) in the source rest frame. [*See the electronic edition of the Journal for a color version of this figure.*]

of X-ray flares, although timescales associated with a single flare are usually shorter. Attributing the whole emission between 4 and 20 ks to a superposition of many flares allows the final drop to be explained with the curvature effect, resetting the reference time t_0 just before the rapid decay. In this case, the smoothness of the flat phase could be a selection effect, due to lacking full coverage of the light curve. The hypothesis of flares blending to form an apparent plateau seems, however, very unlikely, requiring a high degree of homogeneity between successive X-ray flares, since no large-amplitude variations have been observed (see Fig. 2).

We conclude that GRB 070110 robustly suggests new properties of the GRB central engine: it must be able to last for an extended period of time (in this case up to 8×10^3 s in the source rest frame), with an essentially constant radiation power.

Previous *Swift* observations of X-ray flares (Burrows et al. 2005b; Barthelmy et al. 2005b; Falcone et al. 2006; Romano et al. 2006; Campana et al. 2006; Cusumano et al. 2006, 2007) have revealed that the GRB central engine can indeed be active to such a late epoch. However, the energy output (at least the observed luminosity) in previous cases has to be intermittent. The mechanisms to interpret these intermittent X-ray flares therefore require that the central engine accrete episodically, either due to fragmentation or density fluctuation of the accretion disk (e.g., King et al. 2005; Perna et al. 2006; Rosswog 2007), or due to modulation of the magnetic fields near the accretor (Proga & Zhang 2006). Alternatively, the intermittent behavior of the central engine may be related to the unsteady magnetic activity of the central engine (e.g., Dai et al. 2006). None of these suggestions seems to be able to interpret the internal plateau in GRB 070110 straightforwardly. Rather, we require that the central engine be continuously active for a long period of time.

Such long-term central engine activity has been discussed before [e.g., Zhang & Mészáros 2001, for a general discussion of a central engine with decaying luminosity $L(t) \propto t^{-q}$]. The most straightforward example is a spinning-down pulsar (Dai & Lu 1998; Zhang & Mészáros 2001). This model has been introduced to interpret the external plateau as due to refreshed shocks, although those data can be also interpreted without introducing such a long-term central engine (Rees & Mészáros 1998; Granot & Kumar 2006). The discovery of the internal-shock origin of the plateau in GRB 070110 breaks the degeneracy of the refreshed shock interpretation and gives the first direct evidence of a continuous long-lasting central engine.

We propose that the engine powering the plateau could be a spinning-down pulsar that has a constant luminosity lasting for an extended period of time (Shapiro & Teukolsky 1983; Zhang & Mészáros 2001). The duration of the plateau depends on the unknown pulsar parameters, but given a reasonable radiation efficiency, the luminosity ($\sim 10^{48}$ erg s^{-1}) and the observed duration ($\sim$16 ks) of the plateau are consistent with the parameters of a new-born magnetized millisecond pulsar as the GRB central engine.

According to Zhang & Mészáros (2001) the continuous injection luminosity $L_{\rm em,0}$ and the characteristic timescale $\mathcal{T}_{\rm em}$, when the plateau breaks down, are related to the pulsar initial parameters

$$L_{\rm em,\,0} \simeq 10^{49} B_{p,15}^2 P_{0,-3}^{-4} R_6^6 \ {\rm erg\ s^{-1}}, \quad (1)$$

$$\mathcal{T}_{\rm em} \simeq 2.05 \times 10^3 I_{45} B_{p,15}^{-2} P_{0,-3}^{2} R_6^{-6} \ {\rm s}, \quad (2)$$

where $B_p = B_{p,15} \times 10^{15}$ G is the dipolar field strength at the poles, $P_{0,-3}$ is the initial rotation period in milliseconds, I_{45} is the moment of inertia in units of 10^{45} g cm^2, and R_6 is stellar radius in units of 10^6 cm.

If we assume that a significant fraction of the spin-down luminosity is emitted in the X-ray band and take standard values of $I_{45} \sim 1$ and $R_6 \sim 1$, from the plateau parameters we can infer a pulsar initial period of $P_0 \lesssim 1$ ms and a magnetic field $B_p \gtrsim 3 \times 10^{14}$ G. The energy of the plateau puts only a lower limit to the real energy of the central pulsar $L_{\rm em,0}$, and without a good estimate of the radiation efficiency it is not possible to constrain better the pulsar parameters. It is worth noting that our estimate of P_0 is very close to the breakup period for a neutron star, $P_{\rm min} = 0.96$ ms (Lattimer & Prakash 2004), so the derived pulsar parameters can be taken as good approximations of the right values.

The observed decay slope following the plateau is much steeper than the model prediction ($\alpha \sim 2$). However, accounting for detailed energy dissipation mechanisms and possible magnetic field decay at the central engine can steepen the decay (B. Zhang et al. 2007, in preparation). The energy dissipation mechanism of a spinning-down pulsar before deceleration is not well studied, but it may be related to the breakdown of the magnetohydrodynamic condition in the magnetized outflow (Usov 1994; Spruit et al. 2001; Zhang & Mészáros 2002a) and powered by magnetic reconnections (Drenkhahn & Spruit 2002). Instability inside the energy dissipation regions would induce fluctuations in the emission region, giving rise to the flickering light curve and the hardness ratio variations on the plateau.

3.3. *The Final Shallow Decay*

The late X-ray light curve shows a shallow power-law decay on which a flare at $\sim$55 ks and miniflares up to $\sim$200 ks are superposed. These flares could again be interpreted as late central engine activities (Burrows et al. 2005b; Romano et al. 2006; Falcone et al. 2006; Zhang et al. 2006; Fan & Wei 2005) that are likely related to the episodic accretion processes and may be different from the spin-down-powered plateau.

From the SED analysis (§ 2.5) we derived that in the time interval 5–20 ks we observe an internal afterglow component, which contributes strongly to the X-ray but not the optical band, and a second afterglow component, likely of external shock origin, which tracks the optical light curves. This component dominates after the late steep drop, when the emission from the central engine switched off. The late optical/X-ray spectrum ($t = 100$ ks) can be described by a continuous power law ($\beta = 1.00 \pm 0.14$), indicating that the optical and the late X-ray afterglow may arise from the same physical component.

The shallow temporal slopes in the X-ray band ($\alpha_X \sim 0.7$) and in the optical bands ($\alpha_{opt} = 0.63 \pm 0.13$) are consistent. However, we note that the observed temporal decays are not in agreement with the standard closure relations (e.g., Zhang & Mészáros 2004), which predict a temporal slope $\alpha \gtrsim 1$ for both the X-ray and the optical light curves. Such shallow behavior at late times is seen in ~50% of the X-ray light curves observed by *Swift*, as noted by Willingale et al. (2007), and it may suggest that the external shock is kept refreshed by a long-lasting energy injection.

4. CONCLUSION

GRB 070110 is a long burst ($T_{90} \sim 90$ s) with standard behavior in the gamma-ray band that shows extraordinary properties of the X-ray afterglow. The presence of a plateau followed by an unexpected steep decay implies a new emission component from a long-lasting central engine. Such constant emission may be generated by a spinning-down pulsar. This mechanism indeed allows us a better interpretation of the GRB 070110 phenomenology than the superposition of multiple flares. However, the naive picture we discussed cannot account for the rapid decay at the end of the plateau, indicating that a more detailed theoretical study is needed. A drop of the radiation efficiency, caused by the pulsar deceleration, or a decaying magnetic field of the new-born system could help to explain the steep decay rate.

We wish to thank the anonymous referee for his/her careful reading of the paper. We also thank Daniele Malesani and Paolo Pagano for useful discussions and suggestions.

This work is supported at INAF by funding from ASI through grant I/R/039/04 and by COFIN MIUR grant 2005025417, at Penn State by NASA contract NASS5-00136, and at the University of Leicester by the Science and Technology Facilities Council. We gratefully acknowledge the contributions of dozens of members of the XRT team at OAB, PSU, UL, GSFC, and ASDC and our subcontractors, who helped make this instrument possible.

REFERENCES

Arnaud, K. A. 1996, in ASP Conf. Ser. 101, Astronomical Data Analysis Software and Systems V, ed. G. H. Jacoby & J. Barnes (San Francisco: ASP), 17
Band, D., et al. 1993, ApJ, 413, 281
Barthelmy, S. D., et al. 2005a, Space Sci. Rev., 120, 143
———. 2005b, Nature, 438, 994
Burrows, D. N., et al. 2005a, Space Sci. Rev., 120, 165
———. 2005b, Science, 309, 1833
Campana, S., et al. 2006, A&A, 454, 113
Cash, W. 1979, ApJ, 228, 939
Chincarini, G., et al. 2007, preprint (astro-ph/0701450)
Cusumano, G., et al. 2006, Nature, 440, 164
———. 2007, A&A, 462, 73
Dai, Z. G., & Lu, T. 1998, A&A, 333, L87
Dai, Z. G., Wang, X. Y., Wu, X. F., & Zhang, B. 2006, Science, 311, 1127
Dickey, J. M., & Lockman, F. J. 1990, ARA&A, 28, 215
Drenkhahn, G., & Spruit, H. C. 2002, A&A, 391, 1141
Falcone, A. D., et al. 2006, ApJ, 641, 1010
Fan, Y. Z., & Wei, D. M. 2005, MNRAS, 364, L42
Galama, T. J., & Wijers, R. A. M. J. 2001, ApJ, 549, L209
Gehrels, N., et al. 2004, ApJ, 611, 1005
Goad, M. R., et al. 2007, A&A, 468, 103
Granot, J., & Kumar, P. 2006, MNRAS, 366, L13
Hill, J. E., et al. 2006, ApJ, 639, 303
Jaunsen, A. O., Malesani, D., Fynbo, J. P. U., Sollerman, J., & Vreeswijk, P. M. 2007, GCN Circ. 6010, http://gcn.gsfc.nasa.gov/gcn/gcn3/6010.gcn3
Kann, D. A., Klose, S., & Zeh, A. 2006, ApJ, 641, 993
King, A., et al. 2005, ApJ, 630, L113
Kobayashi, S., & Zhang, B. 2007, ApJ, 655, 973
Krimm, H. A., et al. 2007a, GCN Rep. 26
———. 2007b, GCN Circ. 6014, http://gcn.gsfc.nasa.gov/gcn/gcn3/6014.gcn3
Kumar, P., & Panaitescu, A. 2000, ApJ, 541, L51
Lampton, M., Margon, B., & Bowyer, S. 1976, ApJ, 208, 177
Lattimer, J. M., & Prakash, M. 2004, Science, 304, 536
Lazzati, D., & Begelman, M. C. 2006, ApJ, 641, 972
Liang, E. W., et al. 2006, ApJ, 646, 351
Madau, P. 1995, ApJ, 441, 18
Malesani, D., Fynbo, J. P. U., Jaunsen, A. O., & Vreeswijk, P. M. 2007a, GCN Circ. 6021, http://gcn.gsfc.nasa.gov/gcn/gcn3/6021.gcn3
Malesani, D., Jaunsen, A. O., & Vreeswijk, P. 2007b, GCN Circ. 6015, http://gcn.gsfc.nasa.gov/gcn/gcn3/6015.gcn3
Mangano, V., et al. 2007a, A&A, in press (arXiv:/0704.2235)
———. 2007b, ApJ, 654, 403
Mészáros, P., & Rees, M. J. 1997, ApJ, 476, 232
Nousek, J. A., et al. 2006, ApJ, 642, 389
O'Brien, P. T., et al. 2006, ApJ, 647, 1213
Pei, Y. C. 1992, ApJ, 395, 130
Perna, R., Armitage, P. J., & Zhang, B. 2006, ApJ, 636, L29
Perna, R., Lazzati, D., & Fiore, F. 2003, ApJ, 585, 775
Proga, D., & Zhang, B. 2006, MNRAS, 370, L61
Rees, M. J., & Mészáros, P. 1998, ApJ, 496, L1
Rhoads, J. E. 1999, ApJ, 525, 737
Romano, P., et al. 2006, A&A, 456, 917
Roming, P. W. A., et al. 2005, Space Sci. Rev., 120, 95
Rosswog, S. 2007, MNRAS, 376, L48
Sari, R., Piran, T., & Halpern, J. P. 1999, ApJ, 519, L17
Sbarufatti, B., Mangano, V., Mineo, T., Cusumano, G., & Krimm, H. 2007, GCN Circ. 6008, http://gcn.gsfc.nasa.gov/gcn/gcn3/6008.gcn3
Schlegel, D. J., Finkbeiner, D. P., & Davis, M. 1998, ApJ, 500, 525
Shapiro, S. L., & Teukolsky, S. A. 1983, Black Holes, White Dwarfs, and Neutron Stars: The Physics of Compact Objects (New York: Wiley)
Spergel, D. N., et al. 2007, ApJS, 170, 377
Spruit, H. C., Daigne, F., & Drenkhahn, G. 2001, A&A, 369, 694
Starling, R. L. C., et al. 2007, ApJ, 661, 787
Tagliaferri, G., et al. 2005, Nature, 436, 985
———. 2007, Nuovo Cimento, in press (astro-ph/0701591)
Usov, V. V. 1994, MNRAS, 267, 1035
Watson, D., et al. 2006, ApJ, 652, 1011
Waxman, E., & Draine, B. T. 2000, ApJ, 537, 796
Weingartner, J. C., & Draine, B. T. 2000, BAAS, 32, 1466
Willingale, R., et al. 2007, ApJ, 662, 1093
Zhang, B., & Mészáros, P. 2001, ApJ, 552, L35
———. 2002a, ApJ, 581, 1236
———. 2002b, ApJ, 566, 712
———. 2004, Int. J. Mod. Phys. A, 19, 2385
Zhang, B., et al. 2006, ApJ, 642, 354
Zhang, B.-B., Liang, E.-W., & Zhang, B. 2007, ApJ, in press (astro-ph/0612246)